NUMERICAL SCHEME FOR TWO-SCALE MODEL OF LIQUID PHASE EPITAXY

VLADIMÍR CHALUPECKÝ[1]   AND HEIKE EMMERICH[2]

Abstract. We present a numerical scheme and simulations of a two-scale model for liquid phase epitaxy. The model consists of a macroscopic partial differential equation for solute diffusion and advection in the fluid volume, which is coupled to a microscopic phase-field formulation of the classical BCF-model for epitaxy growth. The numerical scheme is solved by the method of lines, where the spatial derivatives are approximated by finite differences. Finally, we present some computational results.

Key words. FDM, method of lines, liquid phase epitaxy, phase field model.

AMS subject classifications. 35K55, 35R35, 65M06, 65M20

1. Motivation. Liquid phase epitaxy (LPE) [2, 17] is a technique for growing thin crystal films from solution. A substrate is introduced into the liquid solution and the film grows by new atoms attaching at the crystalline surface. The classical approach to mathematical modelling of this process is based on the theory of Burton, Cabrera and Frank [3]. In their theory, atoms are first adsorbed to the crystalline surface. Such atoms are called *adatoms*. They diffuse freely along the surface, they can desorb from it back into the solution with probability proportional to $1/\tau^s$ or incorporate themselves permanently into the surface at a step. The concrete mechanism of the surface growth thus depends on the presence or absence of dislocations in the substrate.

In case there are no dislocations, the surface can grow only by nucleation. The surface does not grow or grows very slowly until the supersaturation of the solution is increased above some level. When the concentration exceed this limit value, spontaneous nucleation takes place and random nuclei appear. These provide the necessary growth steps, where adatoms can attach. The growth then proceeds very quickly due to the high supersaturation by successive nucleation and island coalescence.

If dislocations terminating in the surface are present in the crystal lattice of the substrate, they provide a way of controlling the growth as they introduce the growth steps. In this situation, high supersaturations are not necessary to trigger nucleation and the growth can proceed at lower temperatures and supersaturations. Macroscopically, the crystal growth occurs in the direction perpendicular to the substrate, while microscopically, the growth occurs laterally thanks to the addition of new adatoms at edges of steps. This means that the initial morphology and step topology of the substrate influence the growth mechanism. Steps originating from dislocations form spirals or closed loops, which represent the most common growth morphology.

The BCF model can be formulated mathematically as a free-boundary problem

---

[1]Department of Mathematics, Faculty of Nuclear Sciences and Physical Engineering, Czech Technical University, Prague, Czech Republic.
[2]Institute of Minerals Engineering, RWTH Aachen, Germany.
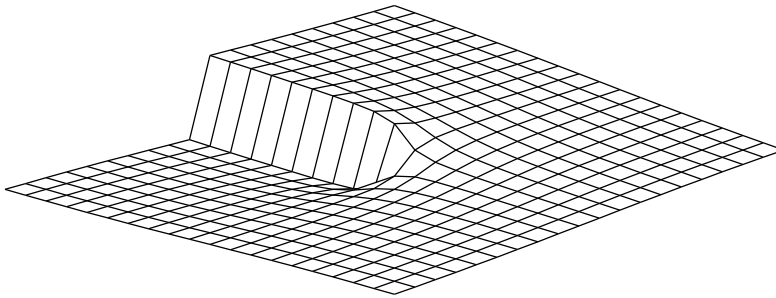
(a) Single screw dislocation
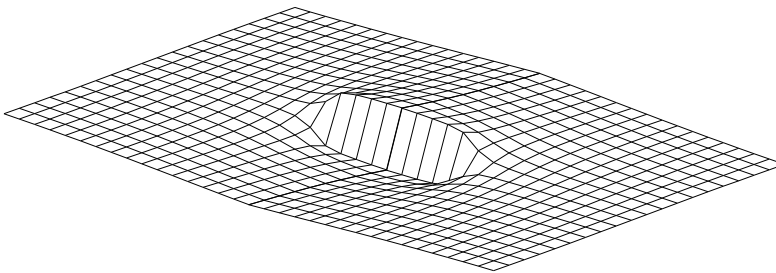
(b) Two screw dislocations of opposite sense connected by a step

Fig. 1.1: *Models of screw dislocations terminating in the crystal surface.*

as

$$\partial_t c^S = D_S \Delta c^S - \frac{1}{\tau_S} c^S + F, \tag{1.1a}$$

$$c^S = c_{\text{eq}}\big(1 + \kappa\Omega\gamma/(k_B T)\big), \ \text{for } t \in (0, T), \ x \in S_0, \tag{1.1b}$$

$$v_\Gamma = D_S \Omega \left[\frac{\partial c^S}{\partial n}\right] \ \text{for } t \in I, \ x \in \Gamma(t). \tag{1.1c}$$

This free-boundary problem is similar to the Stefan problem appearing in solidification (see [18] and references therein). Here, c^S is the density of adatoms on the surface S_0 measured by the number of atoms per unit area, D_S is a surface diffusion coefficient, τ_S is the mean time for the desorption of adatoms from to surface to the solution, F is the deposition rate, c_{eq} is the equilibrium concentration for a straight step, κ is the curvature of step $\Gamma(t)$, Ω is the area of a single atom, γ is the step stiffness, $k_B T$ describes the thermal energy for a fixed temperature T and v_Γ is the normal velocity of the step. The bracket $\left[\frac{\partial c^S}{\partial n}\right]$ denotes the difference of the normal derivative on both sides of the step. Schematic situation of an epitaxial surface submerged in the liquid solution is depicted in Fig. 1.

Direct numerical simulations of the sharp-interface problem (1.1) are difficult, since the position of the steps has to be tracked explicitly. This difficulty can be overcome by using so called phase field method, which has been successfully applied in modelling of many microscopic phenomena. It consists of the introduction of a higher-dimensional order parameter function $\Phi(x, t)$, whose values indicate the phase at a given position. The interface is tracked implicitly and can be recovered as a level
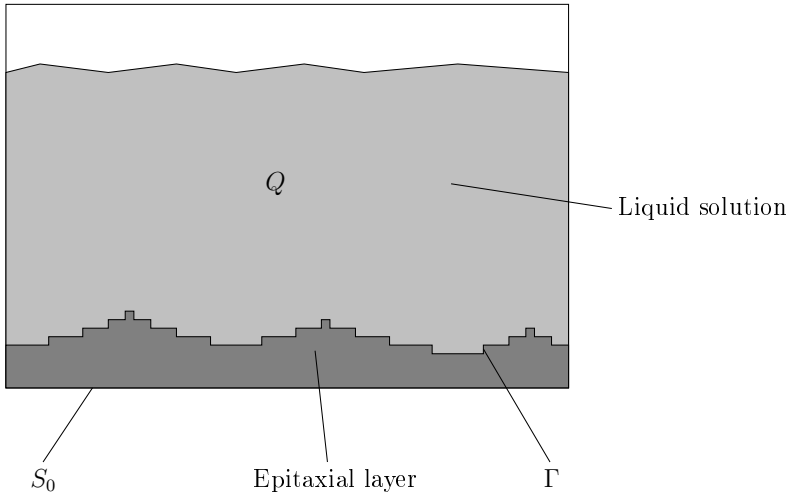
Fig. 1.2: *Vertical cut through the container with liquid solution and epitaxial surface with several spirals placed at the bottom.*

set of Φ at some particular value. In our case, the order parameter will represent the height of the epitaxial surface over the initial substrate profile Φ_s measured by the number of atom layers.

Reformulation of (1.1) as a phase-field model was previously used by Liu and Metiu in [16] for one-dimensional step train. This model was further enhanced by Karma and Plapp in [15] to allow for spiral growth modelling. This model has the form

$$\partial_t c^S = D_S \Delta c^S - \frac{c^S}{\tau_S} + F - \Omega^{-1} \partial_t \Phi, \tag{1.2a}$$

$$\alpha \partial_t \Phi = \xi^2 \Delta \Phi + \sin(2\pi(\Phi - \Phi_s)) + \lambda c^S (1 + \cos(2\pi(\Phi - \Phi_s))), \tag{1.2b}$$

where Φ_s is the height of the initial substrate surface, ξ is a small parameter which describes the width of interfaces (steps) between terraces, α is a time relaxation parameter and λ is a coupling constant. The term $\sin(2\pi(\Phi - \Phi_s)) + \lambda c^S (1 + \cos(2\pi(\Phi - \Phi_s)))$ is a derivative of multi-well potential with minima at integers.

2. Two-scale model of LPE. In LPE systems, unlike systems where the surface grows from vapour, the assumption of quiescent liquid is no longer valid and hydrodynamics effects have to be taken into account. During the crystal growth, concentration near the surface depletes. To prevent this, a forced convection is usually imposed, most often in the form of rotating disk. In this configuration, the liquid solution is drawn to the surface and then expelled in the radial direction parallel to the surface.

Modelling of this process requires dealing with two different scales due to the processes involved. We need to treat the processes taking place on the microscopic scale, where we follow evolution of atom-sized epitaxial layers. At the same time, we want to use continuum models to treat diffusion and fluid flow in the volume of liquid above the surface.

In [5, 6, 10] a two-scale model for such a situation was derived using homogenization techniques. The phase-field formulation of the model consists of a macroscopic diffusion-convection equation

$$\partial_t c^V = D_V \Delta c^V - v \cdot \nabla c^V, \text{ in } Q \subset \mathbb{R}^3 \times (0, T), \tag{2.1a}$$

of the phase-field version of the microscopic BCF model (1.2)

$$\partial_t c^S = D_S \Delta_y c^S + \frac{1}{\tau_V} c^V - \frac{1}{\tau_S} c^S - \Omega^{-1} \partial_t \Phi, \tag{2.1b}$$

$$\tau_\Phi \xi^2 \partial_t \Phi = \xi^2 \Delta_y \Phi - \sin(2\pi(\Phi - \Phi_s)) + \lambda c^S (1 + \cos(2\pi(\Phi - \Phi_s))), \tag{2.1c}$$

to be solved for every $x \in S_0 \times (0, T)$ on a unit cell $Y \subset \mathbb{R}^2$ and of the coupling condition

$$D_V \frac{\partial c^V}{\partial n} = m_A \left(\frac{\bar{c}^S}{\tau_S} - \frac{c^V}{\tau_V} \right), \tag{2.1d}$$

which serves as boundary condition for equation (2.1a) on the part S_0 of the boundary of Q. Here, c^V is the solute concentration in the volume, c^S is the concentration of adatoms on the epitaxial surface, Φ is the height of the surface, Φ_s is the initial height of the substrate, v is a constant velocity field, τ^V is the rate of adsorption of adatoms to the surface, τ^S is the rate of desorption of adatoms from the surface, ξ is the width of the interface between ridges of the spirals, Ω is the adatom area, $\bar{c}^S = \int_Y c^S \, dx$ is the microscopic mean value of c^S over one spiral cell Y.

Since in the discrete case S_0 is formed by a regular grid of points, we join the cells Y to obtain a rectangular domain $S_m = (0, L_1^S) \times (0, L_2^S)$ and solve the equations (2.1c), (2.1b) in this domain. We supplement this system by suitable initial and boundary conditions. In our setting we consider a small sample above the epitaxial surface and we use the following setup.

We consider Q to be a rectangular domain $(0, L_1^V) \times (0, L_2^V) \times (0, L_3^V \subset \mathbb{R}^3$ and we denote its boundaries as Γ_1^V, Γ_2^V, Γ_3^V, Γ_4^V, S_0, Γ_5^V at $x = 0$, $x = L_1^V$, $y = 0$, $y = L_2^V$, $z = 0$, $z = L_3^V$, respectively. This situation is depicted in Fig. 2.1. Then the system (2.1) is supplemented by the following boundary conditions, which hold for all $t \in (0, T)$,

$$c^V(t, x) = c_{\text{in}}^V, \quad x \in \Gamma_1^V, \tag{2.2}$$

$$\frac{\partial c^V}{\partial n}(t, x) = v \cdot \nabla c^V, \quad x \in \Gamma_2^V, \tag{2.3}$$

$$c_V|_{\Gamma_3^V} = c_V|_{\Gamma_4^V}, \tag{2.4}$$

$$\frac{\partial c^V}{\partial n}(t, x) = 0, \quad x \in \Gamma_5^V, \tag{2.5}$$

$$\frac{\partial c^S}{\partial n}(t, x) = \frac{\partial \Phi}{\partial n}(t, x) = 0, \quad x \in \partial S_m. \tag{2.6}$$

The condition (2.2) means constant inflow of macroscopic concentration at the left side of the 3D volume, the condition (2.3) means free outflow of the same at the right face. At the front and back face of the volume we impose periodic boundary conditions, which are described by (2.4), and at the top face we impose zero Neumann
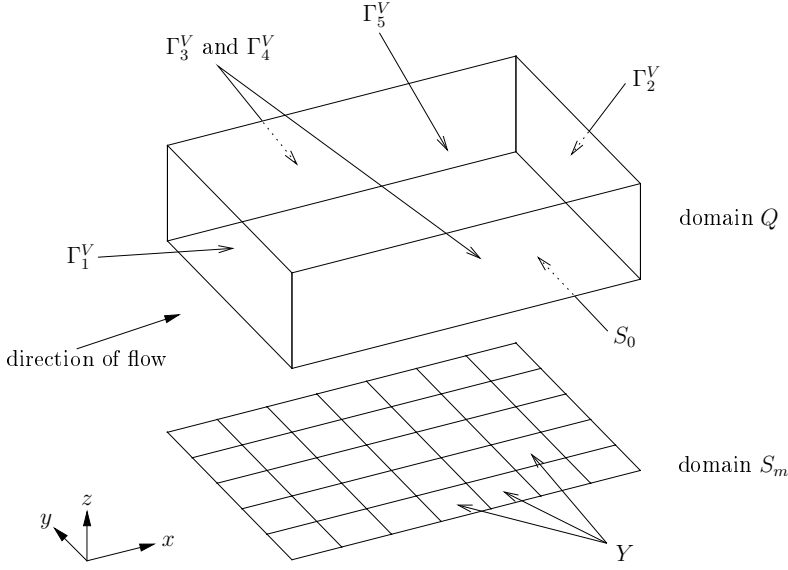
Fig. 2.1: *Notation used for boundaries of Q.*

boundary conditions (2.5). The conditions at the bottom side include coupling to the microscopic problem and are given by (2.1d). At the boundary of S_m we impose zero Neumann boundary conditions (2.6) both for the phase-field and microscopic concentration.

Finally, the initial conditions are given by

$$
\begin{aligned}
c^V(0,x) &= c_0^V(x), \quad x \in Q, \\
c^S(0,x) &= 0, \\
\Phi(0,x) &= \Phi_s(x),
\end{aligned} \quad x \in S_m.
$$

3. Numerical scheme. The scheme we employ for the simulations in Section 5 is based on the method of lines in time. After discretizing the problem by finite differences in space, we solve the resulting ODE system by the standard Runge-Kutta method of fourth order with fixed time step. Application of a variable-step method is not straightforward due to the two-scale nature of the problem and will be addressed in our future work.

Before describing the scheme, we first introduce some notation for the spatial discretization: $h_1^V = \frac{L_1^V}{N_1^V}$, $h_2^V = \frac{L_2^V}{N_2^V}$, $h_3^V = \frac{L_3^V}{N_3^V}$ are the mesh sizes in the volume Q and $h_1^S = \frac{L_1^S}{N_1^S}$, $h_2^S = \frac{L_2^S}{N_2^S}$ are the mesh sizes on the surface S_m, $\omega_h^V = \left\{ (ih_1^V, jh_2^V, kh_3^V) \mid i = 1, \ldots, N_1^V - 1, j = 1, \ldots, N_2^V - 1, k = 1, \ldots, N_3^V - 1 \right\}$ and $\omega_h^S = \left\{ (ih_1^S, jh_2^S) \mid i = 1, \ldots, N_1^S - 1, j = 1, \ldots, N_2^S - 1 \right\}$ are the grids of internal nodes and $\bar{\omega}_h^V = \left\{ (ih_1^V, jh_2^V, kh_3^V) \mid i = 0, \ldots, N_1^V, j = 0, \ldots, N_2^V, k = 0, \ldots, N_3^V \right\}$ and $\bar{\omega}_h^S = \left\{ (ih_1^S, jh_2^S) \mid i = 0, \ldots, N_1^S, j = 0, \ldots, N_2^S \right\}$ are the grids of all nodes.

We can consider grid functions $u : (0,T) \times \omega_h^V \to \mathbb{R}$, $w : (0,T) \times \omega_h^S \to \mathbb{R}$, for which $u_{ijk} = u(t, ih_1^V, jh_2^V, kh_3^V)$ and $w_{ij} = w(t, ih_1^S, jh_2^S)$. We define the standard
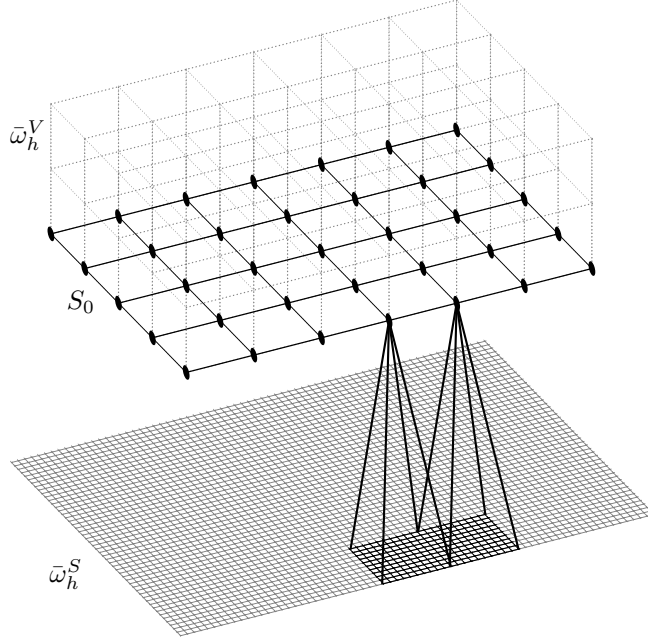
Fig. 3.1: *Relation between the macro grid in 3D and micro grid in 2D.*

central-difference operators

$$\delta_x^c u = \frac{1}{2h_1^V}(u_{i-1,j,k} + u_{i+1,j,k}), \qquad (\delta_x^2 w)_{ij} = \frac{w_{i+1,j} - 2w_{ij} + w_{i-1,j}}{(h_1^S)^2},$$

$$(\delta_x^2 u)_{ijk} = \frac{u_{i+1,j,k} - 2u_{ijk} + u_{i-1,j,k}}{(h_1^V)^2}, \qquad \delta_x^c w = \frac{1}{h_1^V}(w_{i-1,j} + w_{i+1,j}),$$

$$\Delta_h^V u = \delta_x^2 u + \delta_y^2 u + \delta_z^2 u, \qquad \Delta_h^S w = \delta_x^2 w + \delta_y^2 w,$$

$$\nabla_h^V u = (\delta_x^c u, \delta_y^c u, \delta_z^c u).$$

The two meshes $\bar{\omega}_h^V$ and $\bar{\omega}_h^S$ are tightly coupled. At the microscopic surface we model the spiral growth on an array of dislocation cells. The number of these cells in x- and y-direction is the same as the number of grid nodes in x- and y-direction in the macroscopic grid $\bar{\omega}_h^V$, i.e. it is equal to N_1^V, resp. N_2^V. If each cell is discretized by N_1^d nodes in x-direction and by N_2^d nodes in y-direction, then the sizes of the microscopic grid $\bar{\omega}_h^S$ are $N_1^S = N_1^V N_1^d$, $N_2^S = N_2^V N_2^d$. Schematic plot of this situation is shown in Fig. 3.1.

The semi-discrete scheme has the form of

$$\dot{c}_h^V = D_V \Delta_h^V c_h^V - v_h \cdot \nabla_h c_h^V \qquad \text{on } \omega_h^V, \tag{3.1a}$$

$$\alpha\xi^2 \dot{\Phi}_h = \xi^2 \Delta_h^S \Phi_h + \sin(2\pi(\Phi_h - \Phi_h^s))$$
$$+ \lambda_1 c_h^S(1 + \cos(2\pi(\Phi_h - \Phi_h^s))) \qquad \text{on } \omega_h^S, \tag{3.1b}$$

$$\dot{c}_h^S = D_S \Delta_h^S c_h^S + \frac{1}{\tau^V}\bar{c}_h^V - \frac{1}{\tau^S}c_h^S - \frac{1}{\Omega}\partial_t \Phi_h \qquad \text{on } \omega_h^S, \tag{3.1c}$$

where its solution are maps $c_h^V : (0, T) \times \bar{\omega}_h^V \to \mathbb{R}$, $c_h^S : (0, T) \times \bar{\omega}_h^S \to \mathbb{R}$, $\Phi_h : (0, T) \times \bar{\omega}_h^S \to \mathbb{R}$, which also satisfy discrete versions of the boundary conditions and coupling conditions.

The quantities $\bar{u}_h$ and $\bar{c}_h^V$ represent an extension of the macroscopic quantities onto the microscopic mesh $\bar{\omega}_h^S$ so that they are constant on each dislocation cell.

The discretization of the Dirichlet (2.2) and the periodic (2.4) boundary conditions is straightforward, zero Neumann boundary conditions (2.5), (2.6) are treated by mirroring the values in the inner nodes across the boundary. Condition (2.3) is treated specially. The y- and z-components of the discrete gradient operator are computed by taking standard central finite differences in the respective direction. The x-component is computed using the following backward finite-difference operator

$$\delta_x^b u_h|_{i=N_1^V} = \frac{1}{2h_1^V}(u_{N_1^V-2,jk} - 4u_{N_1^V-1,jk} + 3u_{N_1^V jk}), \quad j = 0, \ldots, N_2^V, \ k = 0, \ldots, N_3^V.$$
(3.2)

The coupling condition (2.1d) is discretized using central differences as follows

$$\delta_z^c c_h^V|_{k=0} = \frac{m_A}{D_V}\left(\frac{1}{\tau^S}\bar{c}_{ij0}^S - \frac{1}{\tau_V}c_{ij0}^V\right), \quad i = 0, \ldots, N_1^V, \ j = 0, \ldots, N_2^V.$$
(3.3)

Here,

$$\bar{c}_{ij0}^S = \frac{1}{N_1^d N_2^d}\sum_{lm} c_{lm}^S,$$
(3.4)

where the sum is over the dislocation cell, which corresponds to c_{ij0}^V.

The initial conditions are obtained by projecting the respective functions onto the finite-difference grids. The initial height of the substrate Φ_s is formed by $\arctan(y/x)$ for each dislocation cell, which is properly centered and scaled, so that there is no step between two adjacent spiral cells. This form of Φ_s initiates the spiral growth dynamics.

The ODE system we obtain from (3.1), (3.3) and from the discretized boundary conditions is then solved by the standard Runge-Kutta method of fourth order with fixed time step. Details are given in Algorithm 1.

Algorithm 1 Numerical algorithm for scheme (3.1)

---

1. Set up the constant velocity field v_h.
2. Set up the initial surface Φ^s and initial conditions for c_h^V, c_h^S and Φ_h.
3. Initialize $\partial_t \Phi = 0$.
4. For all the time steps $n = 1, 2, \cdots$
   (a) Compute $\bar{c}_h^S$ by summing over each dislocation cell.
   (b) Extend c_h^V for $k = 0$ onto ω_h^S.
   (c) Compute c_h^V, c_h^S and Φ_h at new time level.
   (d) Compute $\partial_t \Phi_h$ using finite-difference. approximation with Φ_h from the current and previous time step.
   (e) Advance to the next time level.

---

4. Parallel algorithm. For the parallel implementation on distributed-memory systems the Message Passing Interface (MPI) was used. Although in the numerical scheme the finite-difference method was used, the parallel implementation is not

MACRO_COMM

MICRO_COMM

Compute new c_h^V

Compute new Φ_h

Compute $\partial_t \Phi_h$

Send c_h^V at S_0 to MI-CRO_COMM

Receive coupling values from MACRO_COMM

Compute new c_h^S

Receive coupling values from MICRO_COMM

Sum c_h^S over each spiral cell and send values to MACRO_COMM
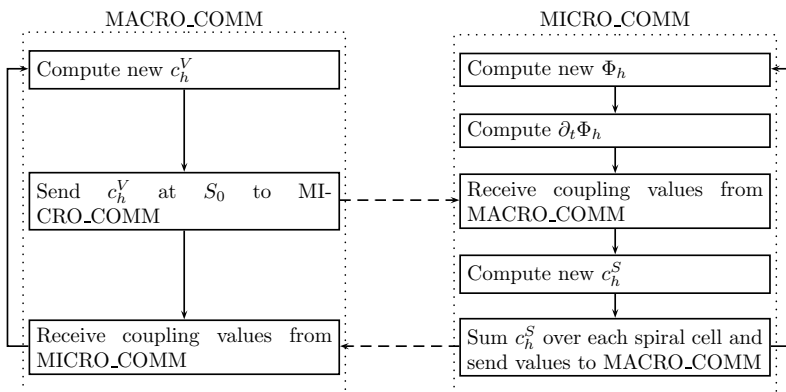
Fig. 4.1: *Outline of the parallel algorithm. Solid arrows denote execution path of the algorithm, dashed line denote data communication between the two MPI communicators.*

straightforward due to two-scale nature of the algorithm. The algorithm proceeds as follows. First, we split the default communicator MPI_COMM_WORLD into two communicators, where one communicator takes care of the microscopic problem and the other of the macroscopic problem. The processors within each group are given Cartesian topology by using functions MPI_Dims_create and MPI_Cart_create. The initialization routine is then finished by various calls to MPI_Cart_shift in order to initialize the communication neighbors of each processor. The master process reads the configuration file with problem parameters and by using MPI_Bcast sends the data to all processors. The main computing loop is outlined in Fig. 4.1. The computing steps are run sequentially within each group, however, each computing step is run in parallel on all available processors in each group. Synchronization within each group occurs when computing boundary conditions, synchronization between the groups occurs when computing the coupling between the microscopic and macroscopic problems.

5. Numerical results. In the numerical experiments we impose a constant velocity field defined as

$$v_{ijk} = \left(v_0 \sqrt{k h_z^V}, 0, 0 \right),$$

where the ijk denote the three spatial directions and h_z^V the mesh size in the z-direction in the volume.

The simulations allow to visualize e.g. how the variation of the macroscopic flow field as depicted in Fig. 5.1 is accompanied by a variation of the concentration field in the melt which in turn results in a systematic variation of micro structure evolution as depicted in Fig. 5.2. Fig. 5.2 displays the micro scale ridges, which wind around the dislocations forming spirals. The height between successive turns of the ridges is one atomic layer. Obviously spirals on the left hand side of the simulated part of the sample, where the macroscopic concentration field due to the dynamics of the transport fields in the volume is largest, grow faster than those on the right hand side of the system. Systematic parameter studies to show the limitations of

previous perturbative studies [14, 7] of micro structure evolution in LPE are still open, just as their analysis to extract relations between processing parameters and morphological stability of the material sample which promise to allow for a desired more efficient parameter control in the sensitive crystallization process of LPE grown material systems [8].
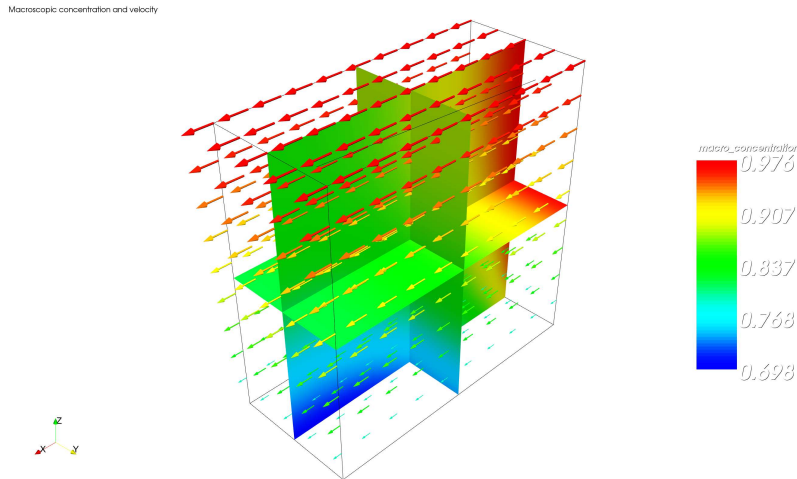
Fig. 5.1: *Dynamics at the macroscale.*
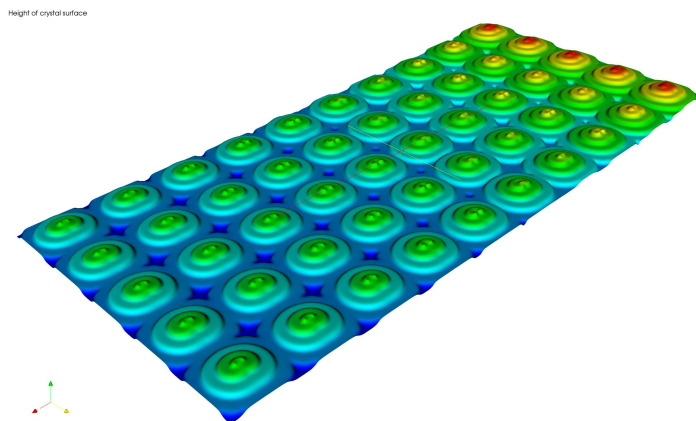
Fig. 5.2: *Dynamics of microstructure evolution.*

Before commenting on the parameters regimes obtained from the numerical simulations, we will introduce an additional quantity characterizing the dynamical aspects of the spiral growth, the so called surface width $w(t)$, which is defined by

$$w(t) = \frac{1}{2}\langle \Phi(x,t)^2 - \langle \Phi(x,t)\rangle^2\rangle^{1/2}, \tag{5.1}$$

where $\langle f \rangle \equiv \int_{S_0} f \; dx$.

The numerical parameters for all the following simulations were set up as follows, if not stated otherwise. The time step size for the Runge-Kutta solver was set to 0.002 and the system was evolved for 400000 time steps, so that $T = 800$. An array of 5×1 dislocations was simulated, each dislocation was discretized on a regular rectangular grid with 60×119 nodes, so the dimensions of ω_h^S were 595×60 and the dimensions of ω_h^V were $5 \times 1 \times 5$. Φ_s was set up so that the dislocations were 10 grid nodes long. The spatial step size for ω_h^S was set to $8/59$, for ω_h^V to 1. The interface width ξ was set to 0.3, the characteristic time of attachment of adatoms α to 1, the coupling constant λ_1 to 10, the desorption rate τ_S to 3.0, the adsorption rate τ_V^0 to 2.0, adatom area Ω to 1.0, the diffusion coefficient D_S to 2.0, D_V to 10 and the mass of an adatom m_A^0 to 0.1.

In the first set of numerical experiments we show the influence of different concentration quantity flowing to the volume from the left (in the form of Dirichlet boundary condition (2.2). In Fig. 5.3 several plots demonstrating the evolution of the surface are shown. At the beginning, the volume is filled with constant concentration equal to the concentration inflow from the left. At the start of the evolution, the leftmost and rightmost spiral grow at almost the same speed. Then, due to the gradual deposition of atoms on the surface, the macroscopic concentration field settles in a steady state profile and maintains it during the rest of the evolution. Owing to this, the first spiral starts to grow faster, as it has more concentration to grow from. The growth of the last spiral is delayed. This causes oscillations in the ratio of w for an inflow value $c_{\mathrm{in}}^V = 0.1$. If we increase c_{in}^V growth proceeds faster. However, the evolution of the surface width displays a universal behaviour independent of the precise value of c_{in}^V in the sense that after an initial transient it increases linearly. Moreover, the ratio of w at the left and right spiral evolves to a constant value.

The effect of velocity profile v on the surface evolution is demonstrated in Fig. 5.4. The same setup as in the previous case was used, the velocity v_0 at the top of the volume is equal to 1. The ratio of w for the left and right spiral again tends to a constant value, which is lower than in the previous case. This is due to the higher velocity, which causes the macroscopic concentration profile to be more uniform.

From these numerical experiments we conclude that as long as we can ensure a quasi-stationary growth dynamics (via our choice of simulation parameters, initial and boundary conditions) the ratio of the surface widths measured over spirals at opposite boundaries of the sample tends to a constant. Moreover, higher velocities yield more uniform distributions of the atoms at the surface along the direction of flow. Consequently, the height of spirals turns out to be more uniform, as well. Finally, higher concentrations of atoms in the liquid volume speed up spiral growth linearly.

6. Conclusion. A two-scale model for liquid phase epitaxy [10, 12] was presented together with a numerical scheme based on the method of lines. Spatial discretization is done by finite differences, in time the model is solved employing the standard Runge-Kutta method of fourth order with fixed time step. Usage of variable-step methods would be beneficial both for accuracy and efficiency, however, their application for the two-scale problem in question is not straightforward due to the difficulties in implementation and local-error estimation.

Systematic parameter studies to show the limitations of previous perturbative studies [14, 7] of microstructure evolution in LPE are work in progress, just as their analysis to extract relations between processing parameters and morphological stability of the material sample which promise to allow for a desired more efficient parameter control in the sensitive crystallization process of LPE grown material systems [8].

(a) $c_{\mathrm{in}}^V = 0.1, \ v_0 = 0.1$

(b) $c_{\mathrm{in}}^V = 1, \ v_0 = 0.1$

(c) $c_{\mathrm{in}}^V = 3, \ v_0 = 0.1$
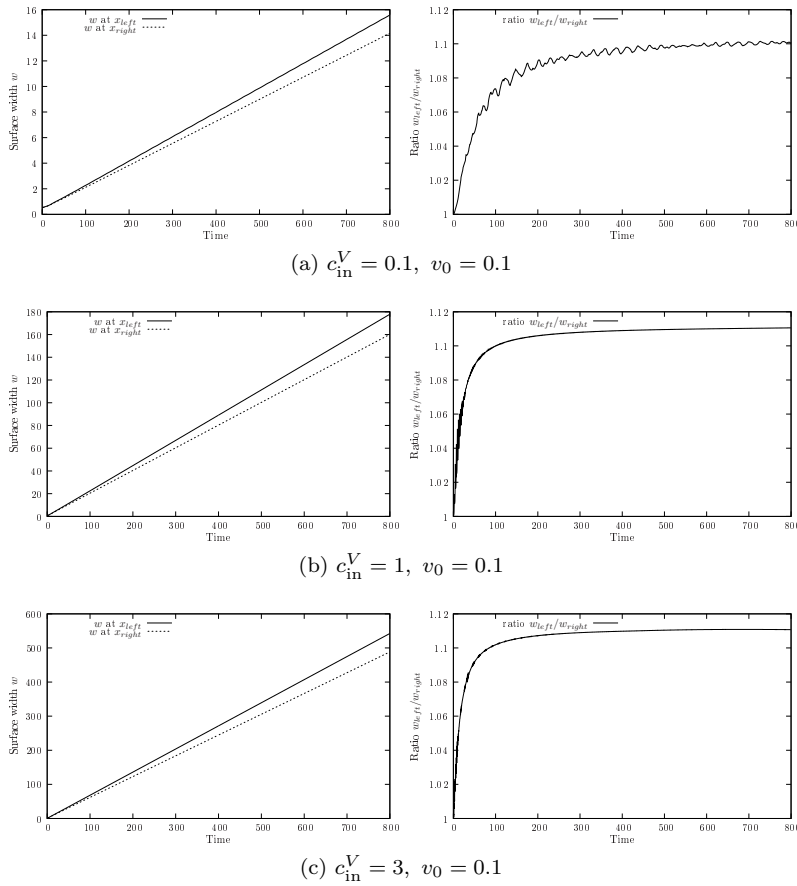
Fig. 5.3: *Comparison of surface dynamics for different levels of incoming concentration at low velocity v. In the left column the surface width at the first and last spiral cell is shown, in the right column the ratio of w between the same two cells is shown. Each row corresponds to a different concentration level.*

REFERENCES

[1] L. Balykov, V. Chalupecký, Ch. Eck, H. Emmerich, G. Krishnamoorthy, A. Rätz, and A. Voigt, Multiscale Modeling of Epitaxial Growth: from Discrete-Continuum to Continuum Equations. In: A. Mielke (ed.), *Analysis, Modeling, and Simulation of Multiscale Problems*, Springer (2006).
[2] E. Bauser, *Atomic Mechanisms in Semiconductor Liquid Phase Epitaxy.* In: D. T. J. Hurle (ed.), Handbook of Crystal Growth, Vol. **3**, North–Holland, Amsterdam (1994).
[3] W. K. Burton, N. Cabrera, and F. C. Frank, *The Growth of Crystals and the Equilibrium Structure of their Surfaces*, Phil. Trans. Roy. Soc. **243** (1951), 299.
[4] G. Caginalp, *An Analysis of a Phase Field Model of a Free Boundary*, Arch. Ration. Mech.

(a) $c_{\mathrm{in}}^{V} = 1,\ v_0 = 1$

(b) $c_{\mathrm{in}}^{V} = 3,\ v_0 = 1$
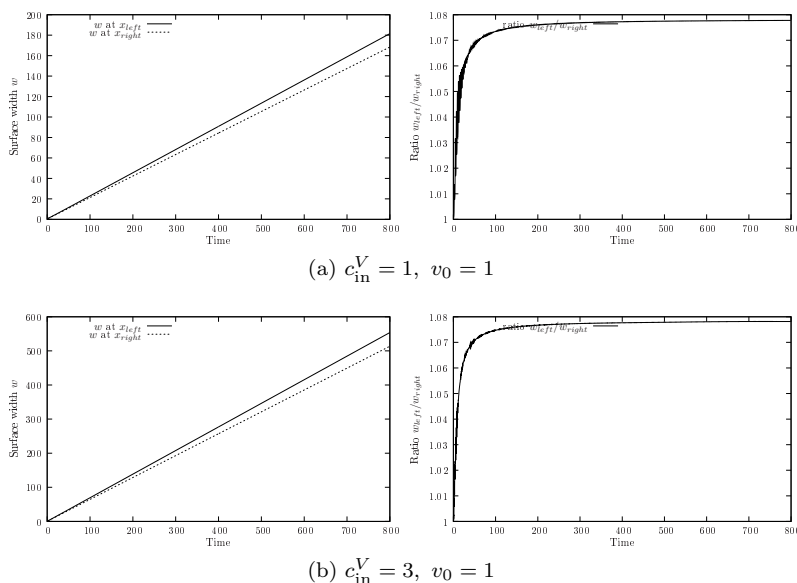
Fig. 5.4: *Comparison of surface dynamics for different levels of incoming concentration at higher velocity v. In the left column the surface width at the first and last spiral cell is shown, in the right column the ratio of w between the same two cells is shown. Each row corresponds to different concentration level.*

Anal. **92** (1986), 205–245.

[5] V. CHALUPECKÝ, CH. ECK, AND H. EMMERICH, *A Two-Scale Model for Liquid Phase Epitaxy*, Preprint 196, SPP 1095 "Mehrskalenprobleme", 2006.

[6] V. CHALUPECKÝ, CH. ECK, AND H. EMMERICH, *A Homogenized Model for Micro-Macro Simulations of Liquid Phase Epitaxy*, submitted to Computer Physics Communications 2007.

[7] A. A. CHERNOV, AND T. NISHINAGA, In: I. Sungawa (ed.), *Growth Shapes and Stability in Morphology of Crystals*, p. 270, Terra Scientific Publ. Co., 1987.

[8] W. DORSCH, S. CHRISTIANSEN, M. ALBRECHT, P. O. HANSSON, E. BAUSER, AND H. P. STRUNK, *Early Growth Stages of $Ge_{0.85}Si_{0.15}$ on Si(001) from Bi solution*, Surf. Sci. **896**, 331, 1994.

[9] CH. ECK, *Analysis of a Two–Scale Phase Field Model for Liquid–Solid Phase Transitions with Equiaxed Dendritic Microstructures*, Multiscale Modeling and Simulation **3**, no. 1 (2004), 28–49.

[10] CH. ECK, AND H. EMMERICH, *Models for Liquid Phase Epitaxy*, Preprint 146, DFG SPP 1095 "Mehrskalenprobleme", 2004.

[11] CH. ECK, AND H. EMMERICH, *Liquid-Phase Epitaxy with Elasticity*, Preprint 197, DFG SPP 1095 "Mehrskalenprobleme", 2004.

[12] CH. ECK, AND H. EMMERICH, *Computation of Nonlinear Multiscale Coupling Effects in Liquid Phase Epitaxy*, submitted to SIAM Multiscale Modeling and Simulation, 2007.

[13] H. EMMERICH, AND CH. ECK, *Morphology–Transitions at Heteroepitaxial Surfaces*, Cont. Mech. Thermodynamics **17** (2006), 373.

[14] L. D. KHUTORYANSKII, AND P. P. PETROV, *Sov. Phys. Crystallogr.* **23** (1978), 571.

[15] A. KARMA, AND M. PLAPP, *Spiral Surface Growth without Desorption*, Phys. Rev. Lett. **81** no. 20 (1998), 4444–4447.

[16] F. LIU, AND H. METIU, *Stability and Kinetics of Step Motion on Crystal Surfaces*, Phys. Rev. E **49** (1997), 2601–2616.

[17] M. B. SMALL, E. GHEZ, AND E. GIESS, Liquid Phase Epitaxy. In: D. T. J. Hurle (ed.), *Handbook of Crystal Growth*, Vol. **3**, North–Holland, Amsterdam, 1994.

[18] A. VISINTIN, *Models of Phase Transitions*, Birkhäuser, Boston, 1996.